

Attitude Estimation and Geometry Reconstruction of Satellite Targets Based on ISAR Image Sequence Interpretation

YEJIAN ZHOU 

LEI ZHANG 

YUNHE CAO

ZHENHUA WU 

Xidian University, Xi'an, China

Analysis of the attitude and geometry of space targets with the inverse synthetic aperture radar (ISAR) technique is a significant and difficult task. Most of the existing methods hardly consider the radar observation geometry in the determination of target attitude. This paper proposes a novel approach to estimating the three-dimensional attitude and reconstructing typical component geometry of space targets from an ISAR image sequence. The approach bridges range-Doppler images and target attitude parameters with the accommodation of target trajectory information and the ISAR geometric projection model. By exploring the shape feature within the ISAR sequence, the target attitude and the rectangular component size are estimated through solving an optimization with prior shape constraints. Comparative experiments illustrate the advantages of the proposed method in both feature association and reconstruction feasibility. Moreover, considering practical circumstances, a further analysis is made of the robustness of the proposed algorithm after the attitude estimation experiment.

Manuscript received March 8, 2018; revised July 12, 2018 and September 24, 2018; released for publication September 28, 2018. Date of publication October 11, 2018; date of current version August 7, 2019.

DOI No. 10.1109/TAES.2018.2875503

Refereeing of this contribution was handled by K. S. Kulpa.

This work was supported in part by the National Natural Science Foundation of China under Grant 61771372 and Grant 61771367 and in part by the National Outstanding Youth Science Fund Project under Grant 61525105.

Authors' addresses: Y. Zhou, Y. Cao, and Z. Wu are with the National Laboratory of Radar Signal Processing and the Collaborative Innovation Center of Information Sensing and Understanding, Xidian University, Xi'an, 710071, China, E-mail: (zhouyedian25@163.com; caoyunhe@mail.xidian.edu.cn; wudoufenglan@163.com); L. Zhang is with the National Laboratory of Radar Signal Processing and the Collaborative Innovation Center of Information Sensing and Understanding, Xidian University, Xi'an 710071, China, and also with School of Electronics and Communication Engineering Sun Yat-Sen University, Guangzhou 510275, China, E-mail: (leizhang@xidian.edu.cn). (*Corresponding author: L. Zhang.*)

0018-9251 © 2018 IEEE

I. INTRODUCTION

The motion state and geometry of satellite targets are important information for analyzing and monitoring their health to ensure availabilities of remote sensing applications [1], [2]. With an increasing number of satellite targets launched on orbit, the analysis task is not limited to detecting and tracking targets. It also includes the information acquisition of the target potential intention and structural integrity, such as the geometrical parameters of pivotal payloads and the attitude information of mounted sensors. In practical applications, these tasks usually rely on long-time observations via radar or optical sensors [3]–[6]. In this paper, we interpret the high-resolution images of satellite targets acquired by ground inverse synthetic aperture radar (ISAR) systems to obtain the attitude and geometric information of satellite targets.

Reviewing its development, the target state analysis technology generally can be sorted into two categories. One basic class works by matching the target features extracted from the observation data or images with a pre-existing database. Maximum likelihood search is usually performed to determine the target attitude. Some radar observations, such as the radar cross section (RCS), the high-resolution range profile, and the ISAR imagery, have been investigated in relevant exploratory works [3]–[14]. In [10], a simulation system was developed to generate full-angle ISAR images under a certain observation geometry, and the target attitude was determined by matching the measured image with the simulation images. This sort of data-driven method performs well in some particular tasks [8]–[10], but the completeness demand of the simulation database would fail its applications in circumstances with efficiency requirements. It should be noted that the assumption of the prior knowledge of the target model is not suitable for some noncooperative targets. Another type of approach is to achieve the three-dimensional (3-D) reconstruction of targets from multiperspective image sequences [15]–[17]. Transferred from computer vision technologies, the singular value decomposition (SVD) is usually adopted to accomplish the structural reconstruction. In [17], SVD was applied to decompose the point-based range-Doppler (RD) history matrix for target 3-D reconstruction. Similar factorization methods were introduced to realize the shape and motion reconstruction of the observed object in [18] and [19]. The core procedure of these methods is to obtain the 3-D reconstruction from the multiperspective observation projection matrices. It should be emphasized that the geometric projections of radar and camera imaging are intrinsically different. As a result, the projection calibration of ISAR imaging cannot be achieved by the successful techniques in optic 3-D reconstruction. Moreover, current methods [17]–[21] for 3-D reconstruction with the ISAR image sequences are based on the precarious scattering point model assumption, which would face the mess of the target scattering sensitivity to the radar line of sight (LOS) (the so-called angular glint phenomenon [22], [23]). This phenomenon is very common in high-frequency radar measurements and makes feature

association among ISAR image frames even more difficult, increasing the failure risk of the factorization method. As a result, the attitude estimation and 3-D reconstruction based on point features will lose their accuracy in practical applications.

In this paper, we propose a three-level processing algorithm to estimate the 3-D attitude and goal component geometric parameters of the satellite target from ISAR image sequences. The algorithm explores the continuous changing of typical rectangular structures among the ISAR image sequence to interpret the attitude information of space targets. This interpretation procedure is deduced with an explicit expression based on the mathematical representation of ISAR imaging projection [24]. Meanwhile, LOS angle parameters are calculated from the target trajectory data. Accommodating the particle swarm optimization (PSO) algorithm [9], [25], [26], the target attitude parameters are retrieved through a minimization with the constraint of target geometric priors. After the attitude estimation, the sizes of typical components mounted on the target are ready to be acquired with another minimization. Compared with those existing methods, the proposed algorithm has some innovations.

- 1) Different from conventional matching methods, the proposed algorithm explores a high-level image feature within the ISAR image sequence. It derives an explicit expression of the extracted feature instead of directly matching it with a pre-existing database. It offers access for monitoring noncooperative space targets when their structural information is partly known or unknown in advance.
- 2) Compared with current factorization-based methods, the proposed algorithm jointly accommodates radar LOS angle parameters and ISAR image sequences to interpret the target 3-D attitude and geometry. Current factorization methods obtain the 3-D point distribution with an uncertain 3-D rotation, which means the recovered attitude and geometry are ambiguous in scale. In our approach, calculated from the target trajectory data, radar LOS angles determine the corresponding RD imaging planes in the target Cartesian coordinates. Therefore, a series of imaging projection matrices can be built to bridge the image sequence and target attitude parameters in this coordinate system, which facilitates the approach to the ISAR imaging physical mechanism. The obtained optimization parameters can be converted into a definite vector directly to reflect the target absolute attitude in the target Cartesian coordinates.
- 3) From the aspect of image feature extraction, a robust high-level feature is presented to replace the customary scattering point features. Based on the Radon transform, we design a parallelogram descriptor to extract the rectangular component of satellite targets among RD image frames. Utilizing this sort of high-level features for target description avoids the association difficulty caused by the angular glint phenomenon. As a result, planar components like solar wings are automatically

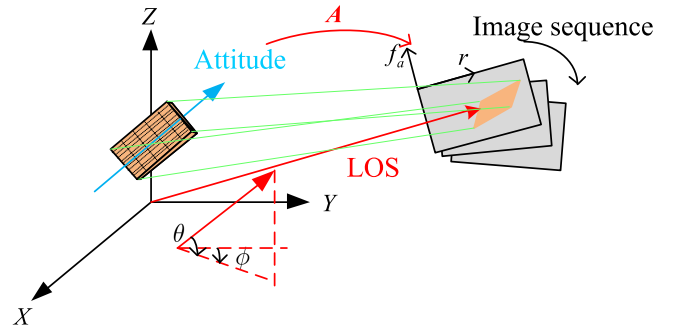


Fig. 1. Motion and geometric projection of ISAR imaging.

associated among the ISAR image sequence. In the 3-D information inversion, we impose target structural priors as a constraint, which ensures that the extracted shape features of rectangular components can be utilized to recover the 3-D construction without losing the structural integrity.

The following contents of this paper are organized as follows. In Section II, a detailed description of the existing problem and the ISAR imaging projection model are presented. In Section III, the implementation details of the proposed algorithm are provided. Section IV is the experimental part, including descriptor comparison, attitude and size parameter estimation, and result analysis. In the final section, some crucial conclusions of this work are given.

II. PROBLEM DESCRIPTION AND THE MATHEMATICAL MODEL

The crux of this research is to bridge the observation ISAR image sequence and the target attitude. According to the ISAR imaging projection theory, the imaging procedure of satellite targets is to project 3-D scattering points on a two-dimensional (2-D) radar imaging plane [24]. This physical interpretation makes it possible to determine the 3-D coordinates of the target from a 2-D ISAR image sequence when the radar observes targets from sufficient viewing angles. As shown in Fig. 1, the mathematical representation of the imaging procedure can be described with a 2×3 matrix \mathbf{A}_f in the target Cartesian coordinates

$$\mathbf{A}_f = \begin{pmatrix} \vec{\mathbf{m}}_f \\ \vec{\mathbf{n}}_f \end{pmatrix} \quad (1)$$

$$\begin{pmatrix} r_{fp} \\ d_{fp} \end{pmatrix} = \mathbf{A}_f (x_p, y_p, z_p)^T = \begin{pmatrix} \vec{\mathbf{m}}_f \\ \vec{\mathbf{n}}_f \end{pmatrix} (x_p, y_p, z_p)^T \quad (2)$$

where subscript f represents the serial number of ISAR images, subscript p represents the serial number of scattering points, (x, y, z) is the point's position in the target Cartesian coordinate system, and $(r_f, d_f)^T$ refers to the point's position in the RD imagery. Direction vectors $\vec{\mathbf{m}}_f$ and $\vec{\mathbf{n}}_f$ determine the range axis and the Doppler axis of imaging projection in the target Cartesian coordinates, respectively.

In most of the current factorization methods, these projection matrices are considered as unknown factors [18]–[22], and (2) is described in the matrix formulation as follows:

$$\mathbf{W} = \mathbf{RS} \quad (3)$$

$$\mathbf{W} = \begin{pmatrix} r_{11} \dots r_{1p} \\ \vdots \\ r_{f1} \dots r_{fp} \\ d_{11} \dots d_{1p} \\ \vdots \\ d_{f1} \dots d_{fp} \end{pmatrix}, \mathbf{R} = \begin{pmatrix} \vec{\mathbf{m}}_1 \\ \vdots \\ \vec{\mathbf{m}}_f \\ \vec{\mathbf{n}}_1 \\ \vdots \\ \vec{\mathbf{n}}_f \end{pmatrix}, \mathbf{S} = \begin{pmatrix} x_1 \dots x_p \\ y_1 \dots y_p \\ z_1 \dots z_p \end{pmatrix}. \quad (4)$$

Under the constraint of the vertical relationship between the range axis and the Doppler axis [see (7)], the RD history matrix is decomposed via the SVD algorithm [17], [18], [20]

$$\mathbf{W} = \bar{\mathbf{U}} (\mathbf{C} \mathbf{C}^{-1}) \bar{\mathbf{Q}}^T = (\bar{\mathbf{U}} \mathbf{C}) (\mathbf{C}^{-1} \bar{\mathbf{Q}}^T) = \tilde{\mathbf{R}} \tilde{\mathbf{S}} \quad (5)$$

$$\|\vec{\mathbf{m}}_f\| = 1 \quad (6)$$

$$\vec{\mathbf{n}}_f \bullet \vec{\mathbf{m}}_f = 0 \quad (7)$$

where \bullet represents the inner product operation of two vectors, $\bar{\mathbf{U}}$ and $\bar{\mathbf{Q}}$ are two intermediate matrices in the SVD process, and \mathbf{C} is an uncertain Euler rotation matrix. For any such \mathbf{C} , $\tilde{\mathbf{S}} = \mathbf{C}^{-1} \bar{\mathbf{Q}}^T$, is a possible solution for the 3-D coordinate matrix \mathbf{S} , which means utilizing factorization methods to determine the position of each scatter center needs additional rotation calibration.

Therefore, as mentioned above, there are two main drawbacks in interpreting radar images by factorization methods.

- 1) The 3-D reconstruction of factorization methods would be successful only if some conditions are satisfied, such as sufficient scattering points and their distribution. Due to the scattering anisotropy, extracting isolated scattering points can hardly meet the stability demands in practical applications.
- 2) The projection calibration is not readily available for the ISAR image sequence, due to the geometrical character of the radar imaging. This phenomenon is intrinsically different from the camera projection calibration [15], [16]. In order to illustrate the imaging projection difference between these two sensors, the projection comparison is provided in Fig. 2. Obviously, the optic imaging geometry ensures that each optics image contains 3-D information (vertical axis u , horizontal axis v and deep axis $depth$), while each radar image only contains 2-D information (range axis r and Doppler axis f_a). As a result, the recovery problem of the target attitude information is ill-posed and difficult to solve without knowing the RD projection matrices.

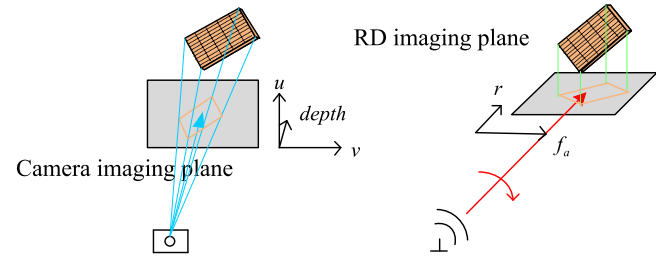


Fig. 2. Imaging planes of ISAR system and optics sensor.

The RD projection matrices bridge RD images with the target geometry. When the attitude of target is assumed stable during the observation, the change of the target projection in RD planes only depends on instantaneous radar LOS angles, which can be directly obtained from the radar tracking system [27]–[29]. The assumption of target attitude stabilization refers to that the same part of the satellite (i.e., the solar wing) is always pointing toward a specific direction in the target Cartesian coordinates for astrodynamics reasons. It is confirmed by practical observations for some typical in-orbit satellites [41], [42].

In this work, we take two LOS angle parameters to express the radar sight direction unit vector in the target Cartesian coordinates by the following equation:

$$\vec{\mathbf{k}}_{\text{LOS}} = (\cos \theta \sin \phi, \cos \theta \cos \phi, \sin \theta)^T \quad (8)$$

where the elevation angle θ is the angle between the instantaneous radar LOS vector and the xOy plane, and the azimuth angle ϕ is the angle between the y -axis and the projection of the instantaneous radar LOS vector in the xOy plane, as shown in Fig. 1.

We can utilize $\vec{\mathbf{m}}_f$ and $\vec{\mathbf{n}}_f$ to determine the RD plane as (9) and (10). In this way, the RD image of the observed target can be represented by projecting scattering points from the 3-D target coordinate into the range and Doppler directions according to (2). In brief, utilizing imaging projection geometry to recover the target's 3-D information is a significant difference between the proposed method and existing factorization methods

$$\vec{\mathbf{m}}_f = \left(\frac{\cos \theta \sin \phi}{\Delta r}, \frac{\cos \theta \cos \phi}{\Delta r}, \frac{\sin \theta}{\Delta r} \right) \quad (9)$$

$$\vec{\mathbf{n}}_f = \left(-\frac{-\sin \theta \sin \phi \theta' + \cos \theta \cos \phi \phi'}{\Delta f_a}, \frac{-\sin \theta \cos \phi \theta' + \cos \theta \sin \phi \phi'}{\Delta f_a}, -\frac{\cos \theta \theta'}{\Delta f_a} \right) \quad (10)$$

where Δr denotes the range resolution, Δf_a denotes the Doppler resolution, θ' represents instantaneous elevation velocity of the radar LOS, and ϕ' represents instantaneous azimuth velocity of the radar LOS.

By calculating the projection matrices, target attitude parameters are ready to be solved if scattering points can be exactly associated between different RD image frames. And another real phenomenon is that some typical components

mounted on targets, like solar wings and plane antennas, usually have a rectangular plane structure. The boundary of the structure is projected as a parallelogram in the RD imaging plane. This robust shape feature has potential to support automatic extraction and can be accommodated to estimate the attitude and geometric parameters of components. Therefore, we analyze the rectangular component in this work. The absolute attitude of the rectangular component reflects important operation and motion states of the target, and the size estimation helps us analyze the structural integrity of the target.

For a clear description of the target attitude estimation, we use two 3-D vectors to represent the attitude vectors of the rectangular component's edges. Based on certain radar LOS angles, the projection equation of them in ISAR imagery can be described as follows:

$$\begin{pmatrix} \sin \psi_{i,f} \\ \cos \psi_{i,f} \end{pmatrix} = \mathbf{A}_f \vec{\mathbf{k}}_i \quad (11)$$

$$\vec{\mathbf{k}}_i = (\cos \alpha_i \sin \beta_i, \cos \alpha_i \cos \beta_i, \sin \alpha_i)^T \quad (12)$$

where subscript $i = L, D$ represents the long edge and the short edge of the rectangular component, respectively, ψ denotes the orientation of each edge in the RD image, and attitude angles α and β are defined in the same way as the radar LOS angles θ and ϕ . The manifold of the projection matrix A_f reflects the angular diversity of the ISAR image sequence, which is crucial to the success of the target attitude determination. In general, long-time observations can provide sufficient angular diversity of the ISAR image sequence.

III. THREE-LEVEL INTERPRETATION ALGORITHM

A. Algorithm Flowchart

Following the previous analysis, a three-level interpretation algorithm for estimating the target attitude and typical component sizes from the ISAR image sequence is introduced in this section. In the approach, necessary information is assumed to be given beforehand;

- 1) the range resolution and Doppler resolution of each image, which depend on the ISAR system and observation geometry;
 - 2) radar LOS angle parameters of each ISAR image, which are loaded from the radar tracking system.

As shown in Fig. 3, the method takes the shape priors of typical rectangular components into account and is realized by the following steps.

Step 1: Adopt the RD algorithm to obtain a high-resolution image sequence of the observed satellite target from radar echoes.

Step 2: Utilize the background segmentation and morphology techniques to extract the target boundary in each ISAR image.

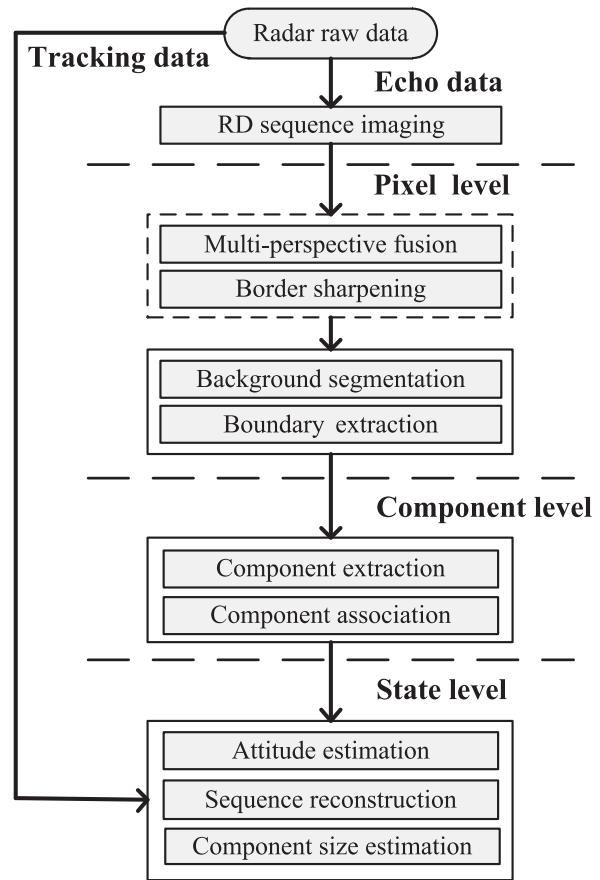


Fig. 3. Flowchart of the proposed approach.

Step 3: Extract typical rectangular components in boundary images and represent them with the proposed parallelogram descriptor.

Step 4: Record the orientation and position parameters of these components to achieve the feature association among the image sequence.

Step 5: Build the RD projection matrix of each ISAR image with the corresponding radar LOS angles, and estimate component attitudes based on the geometric projection model.

Step 6: Estimate component size parameters to evaluate the target state via image sequence reconstruction.

The details of key steps are given in the following subsections.

B. RD Image Sequence Generation

First, a high-resolution image sequence is generated with the RD algorithm [31]. In order to meet the resolution requirements, the radar observation ought to be divided into several segments corresponding to the optimal coherent processing interval (CPI). The division principle is limited to the radar LOS stationary assumption as follows: The LOS angle velocity parameters, θ' and ϕ' , should approximate to constants during the single data segment for the requirement of the 2-D-turnable imaging model. In practice, this requirement can hardly be met, and an acceptable

compromise is that the changing rates of θ' and ϕ' should be within definite thresholds. Besides, we set the single segment as long as possible to pursue high-resolution and well-focused RD images [30], [31]. The detailed discussion of the optimal CPI principle is given in the Appendix.

C. Boundary Extraction From the ISAR Image Sequence

After the RD imaging, some low-quality images in the ISAR image sequence can be managed with image enhancement techniques, such as boundary sharpening and multi-perspective fusion [32]–[34]. It ensures the consistency of image quality for the joint interpretation of the ISAR image sequence in later steps. Then, the target can be effectively segmented out from the entire image with the assistance of background segmentation methods. Furthermore, the enhanced target boundary can be extracted via morphology technologies, like closing operation [34].

D. Automatic Rectangular Component Extraction and Shape Descriptor Fitting

It is an innovation of this paper to seek a robust image feature instead of using the point feature. In practice, the connection between the image feature and target 3-D structural characteristics determines the reliability of corresponding feature descriptor. The feature extraction result directly impacts the performance of the target state analysis. Due to the fact that most of the satellite targets mount rectangular components, like solar wings, we extract and fit them with a novel parallelogram descriptor among the image sequence. The details of the component extraction and shape fitting are given as follows.

Step I: Radon transform is first applied to the target boundary image [35]. Lines with similar orientations in the image will be recorded as pairs.

Step II: Search the long edges of the rectangular component in these line pairs. Normally, the long edges cover most of the boundary points or correspond to the biggest Radon transform value.

Step III: Based on Radon parameters (including orientation and position parameters) of the line pairs, search the points which are lying on and between them as the unfitted component boundary.

Step IV: The unfitted component boundaries will be integrated with Radon transform again. After that, add the two peaks of Radon transform in the same orientation parameter to represent the confidence of the long-edge orientation $\hat{\psi}_{L,f}$.

Step V: Determine the orientation and position parameters of long edges with the biggest confidence value.

Step VI: Similarly, remove points lying on long edges, and the short-edge orientation $\hat{\psi}_{D,f}$ and position can also be detected in the same way (Steps IV and V).

Step VII: Calculate four intersection points of these two line pairs as four vertexes of the parallelogram.

Step VIII: Output edge orientations and vertexes of the parallelogram.

Besides, the parallelogram extraction result in the former image can be utilized for component extraction and shape fitting in the current image. In this way, the goal component will be automatically described as a parallelogram with the long-edge orientation, the short-edge orientation, and four vertexes in each ISAR image frame.

E. Target Attitude Estimation

In this section, we build a series of ISAR imaging project matrices to estimate the target's 3-D attitude from the automatic extraction results of the rectangular components. Before the attitude estimation, image feature association is inevitable to track the components among the image sequence. The association of scattering points among an ISAR observation sequence is usually a difficult task due to the angular glint phenomenon. By contrast, the proposed parallelogram feature descriptor realizes a component-level association to avoid the angular glint problem. Even with occlusion or deformation, the orientation and position parameters of the parallelogram are sufficient to associate the rigid motion of the rectangular component among the ISAR image sequence. A normalized judgment function for the edge association is defined as follows:

$$J(i, j) = a_1 |\hat{\psi}_i - \hat{\psi}_j| + a_2 \| \text{center}_i - \text{center}_j \|_2 \quad (13)$$

where subscript $i = L, D$, $j = L, D$ represent the long and short edges in the current image and the former, respectively, center denotes the center position of the edges (which can be calculated from the vertexes), and a_1 and a_2 denote weight factors, which balance the confidence of different features. In most of the cases, the length of long and short edges changes smoothly across neighboring images. Thus, the association of the long and short edges can be achieved during the component extraction through length identification.

Once the feature association is accomplished, component attitude parameters can be estimated in a minimization [see (14)]. It is built on the observation geometry and takes the structural constraint of rectangular components into account

$$\begin{aligned} & \min_{\alpha_L, \alpha_D, \beta_L, \beta_D} \sum_{f=1}^F \left\| \mathbf{A}_f \vec{\mathbf{k}}(\alpha_L, \beta_L) - (\sin \hat{\psi}_{Lf}, \cos \hat{\psi}_{Lf})^T \right\|_2 \\ & + a_3 \left\| \mathbf{A}_f \vec{\mathbf{k}}(\alpha_D, \beta_D) - (\sin \hat{\psi}_{Df}, \cos \hat{\psi}_{Df})^T \right\|_2 \\ & \text{s.t. } \tan \alpha_L \tan \alpha_D = -\cos(\beta_L - \beta_D) \end{aligned} \quad (14)$$

where $-90^\circ \leq \alpha_i \leq 90^\circ$ and $0^\circ \leq \beta_i \leq 180^\circ$. The optimal selection of a_3 aims to ensure the accuracy of the attitude estimation. Since the long-edge extraction is usually more accurate than the short one, the confidence factor would be set at a relatively small value to enhance the contribution of the long edge in the attitude estimation.

In this paper, the classical PSO algorithm is utilized to solve the optimization [see (14)]. In detail, the solution of the minimization is defined as the particle position in the

PSO algorithm [9], [25], [26]

$$X_i = (\alpha_L, \beta_L, \alpha_D, \beta_D)^T. \quad (15)$$

Based on the structural constraint of rectangular components, the fitness function of the PSO algorithm is defined as (16)

$$\begin{aligned} J = \sum_{f=1}^F & \left(\left\| \mathbf{A}_f \vec{\mathbf{k}}(\alpha_L, \beta_L) - (\sin \hat{\psi}_{Lf}, \cos \hat{\psi}_{Lf})^T \right\|_2 \right. \\ & + a_3 \left\| \mathbf{A}_f \vec{\mathbf{k}}(\alpha_D, \beta_D) - (\sin \hat{\psi}_{Df}, \cos \hat{\psi}_{Df})^T \right\|_2 \Big) \\ & + a_4 F (\tan \alpha_L \tan \alpha_D + \cos(\beta_L - \beta_D)) \end{aligned} \quad (16)$$

where the confidence factor a_4 is uniformly distributed within $[0, 1]$, which enhances the rectangle property of the goal component. The setting principles of a_3 and a_4 depend on the accuracy of previous parallelogram extraction. Empirically, a_3 is set to be 0.6 and a_4 is set to be 0.95 in the experiments.

In the PSO algorithm, the velocity and position variables are iteratively updated according to the swarm search and particle search experiences. The swarm search experience is the best position Gbest found by the swarm, and the particle search experience is the best position Pbest found by the particle. The classical updating rules are provided with (17) and (18).

$$\begin{aligned} V_i(t+1) = & a_5 V_i(t) + a_6 \text{rand}_1 (\text{Pbest} - X_i(t)) \\ & + a_7 \text{rand}_2 (\text{Gbest} - X_i(t)) \end{aligned} \quad (17)$$

$$X_i(t+1) = X_i(t) + V_i(t) \quad (18)$$

where $V_i(t)$ and $X_i(t)$ are the velocity and position of the i th particle in the iteration t ; a_6 and a_7 are two learning rate weights that balance contributions of the self-cognitive and social influence; rand_1 and rand_2 are two random parameters uniformly distributed within $[0, 1]$; a_5 is the inertia weight, and a relatively large inertia weight is better for the global search, while a small weight is better for the local search.

A brief flow of the PSO algorithm is given as follows.

Step I: Generate the particle swarm by randomly sampling of the solution space of the minimization [see (14)]. Then, search Gbest and Pbest.

Step II: Update velocity and position of each particle based on (17) and (18).

Step III: Calculate the fitness value of each particle according to (16), and update Gbest and Pbest. If the maximum iteration or minimum error criterion is satisfied, break the current iteration and turn to Step IV; otherwise, turn to Step II. The minimum error criterion refers to the minimum moving distances of Gbest and Pbest, which depend on the swarm scale and the learning rate in the updating rules.

Step IV: Output the position of the ideal particle, $\tilde{X} = (\tilde{\alpha}_L, \tilde{\beta}_L, \tilde{\alpha}_D, \tilde{\beta}_D)^T$.

In this manner, the component attitude parameters are estimated and will be converted to 3-D vectors according

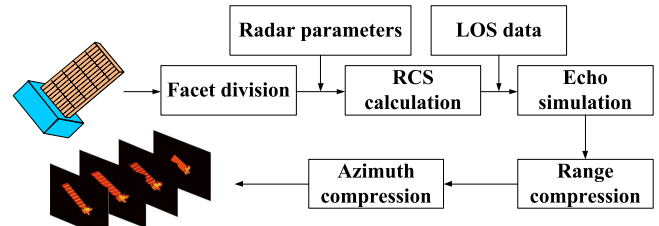


Fig. 4. Flowchart of image sequence simulation.

to (12). The PSO algorithm, the biggest computational burden of the proposed method, will be performed twice in this paper, including attitude optimization and size optimization. The time complexity and space complexity of the PSO algorithm are $O(n^2)$ and $O(n)$, respectively.

F. Image Sequence Reconstruction and Component Size Estimation

In the last step, we attempt to utilize the image sequence reconstruction to estimate the sizes of rectangular components. In this step, besides the attitude estimation result, the extraction result of component positions is also taken into consideration. As we know, previous attitude estimation relies on the connection between the imaging projection geometry and the ISAR image sequence. Fortunately, it corresponds to a one-to-one mapping. In other words, if the target's 3-D model and LOS angles are given, we can reconstruct the image sequence with the estimated attitude parameters. The reconstruction method is similar to the RD image simulation in later experiments [36], [37]. Based on the reconstruction result, size parameters of the typical component can be estimated by minimizing the difference between the reconstructed component image sequence and the original image sequence. The minimization is described as follows:

$$\min_{l_L} \sum_{f=1}^F \left\| l_L \mathbf{A}_f \vec{\mathbf{k}}(\tilde{\alpha}_L, \tilde{\beta}_L) - \text{length}_{L|f} \right\|_2 \quad (19)$$

$$\min_{l_D} \sum_{f=1}^F \left\| l_D \mathbf{A}_f \vec{\mathbf{k}}(\tilde{\alpha}_D, \tilde{\beta}_D) - \text{length}_{D|f} \right\|_2 \quad (20)$$

where l_L and l_D denote size parameters of the rectangular component, and $\text{length}_{L|f}$ and $\text{length}_{D|f}$ are the observation lengths of the rectangular component in the original image sequence, which are solved by parallelogram vertices mentioned above. An alternative method is to manually extract $\text{length}_{L|f}$ and $\text{length}_{D|f}$ among ISAR images when the structural characteristic of the target is complex.

With the accommodation of the PSO algorithm, the component size optimization can be solved in a way similar to the attitude optimization [see (14)]. It ought to be noted that although the estimation error of attitude parameters leads to accessory error in size estimation, the structural information from size estimation result still helps observers analyze the structural integrality of the space target.

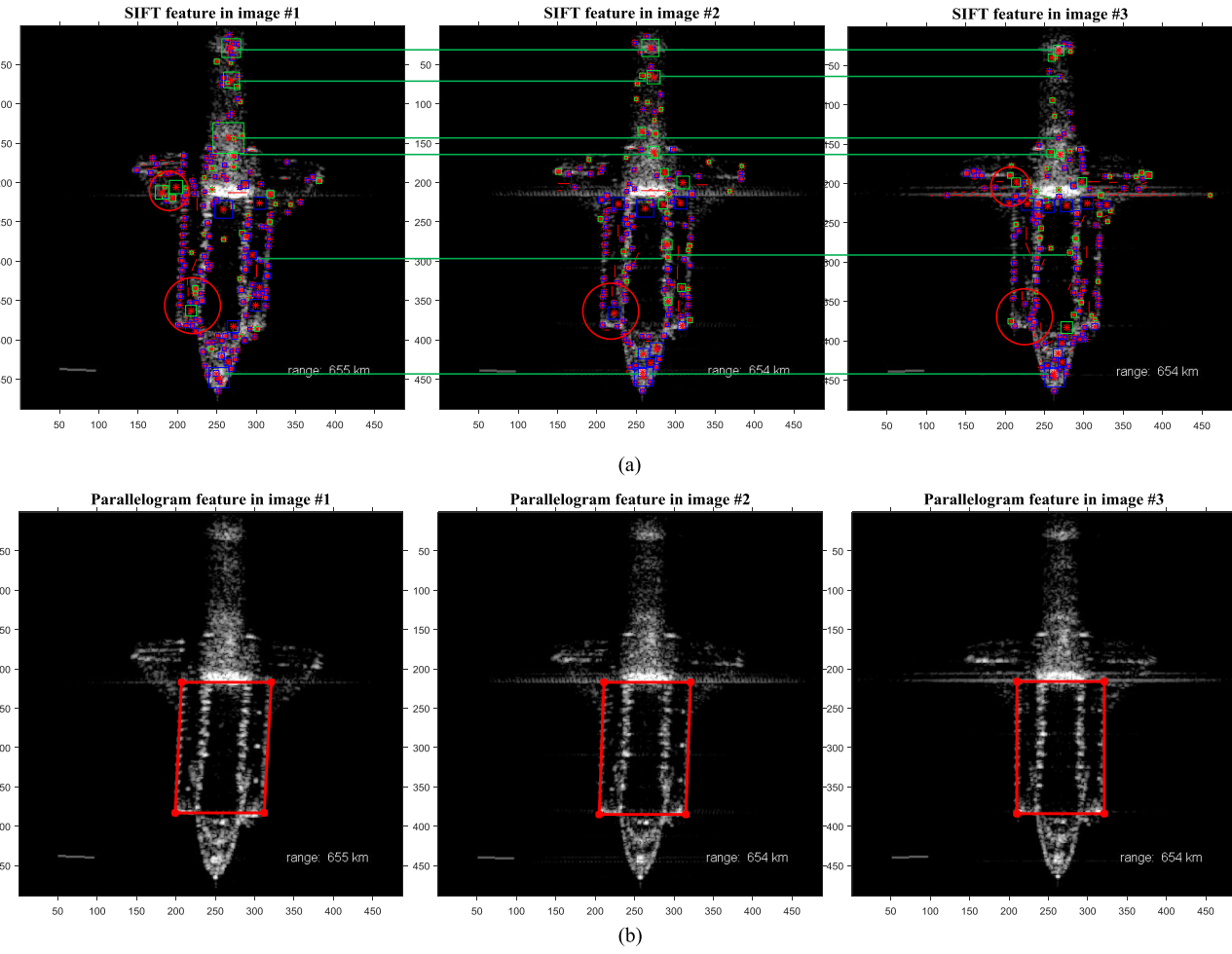


Fig. 5. Comparison of different feature extraction results. (a) SIFT feature extraction result of measured image sequences. (b) Parallelogram feature extraction result of measured image sequences.

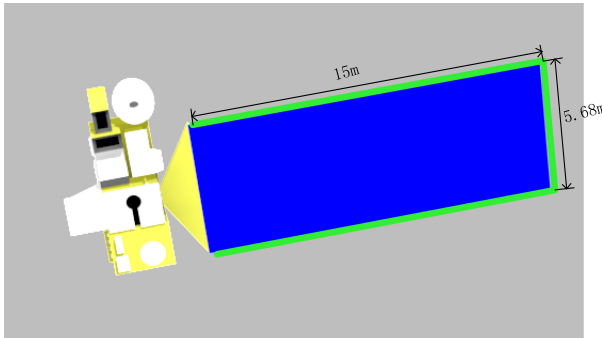


Fig. 6. Three-dimensional model of the Aura Satellite.

IV. EXPERIMENTAL ANALYSIS

In order to highlight the contributions of this paper, we perform different experiments to show its superiority from different aspects. The experiment environment and experiment contents are listed as follows.

Part A: To explain the mess of the image feature extraction in practical applications, we adopt a measured image sequence to compare the image process stability of the

proposed descriptor and the conventional scattering point descriptor in the first part.

Part B: Then, we analyze how the feature extraction result affects the reconstruction result based on the factorization algorithm with a simulated image sequence.

Part C: In the last part, we utilize the proposed three-level interpretation algorithm to estimate the attitude and size parameters of the rectangular component with two simulated ISAR image sequences. The experiment result proves the effectiveness of the proposed method.

Image sequences acquisition: The measurement image sequence adopted in Part A was published by German FGAN Lab in 2012 (@ Fraunhofer FHR). The simulated image sequences used in Parts B and C are conducted in a Windows 7 Professional environment utilizing two-core processors with Intel(R) Xeon (R) CPU E5-2603 v3, 1.60 GHz, 128-GB RAM and the codes are implemented in MATLAB R2015b. A brief infographic representation of the image sequence simulation is depicted in Fig. 4 [36], [37]. In Part B, the central position of divided facets is used as pointwise scatterers to generate point-cloud images, and

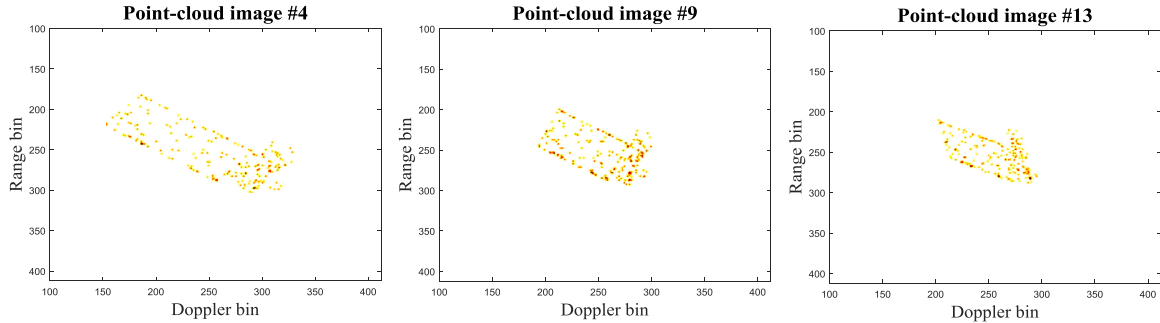


Fig. 7. Observation point-cloud image sequence.

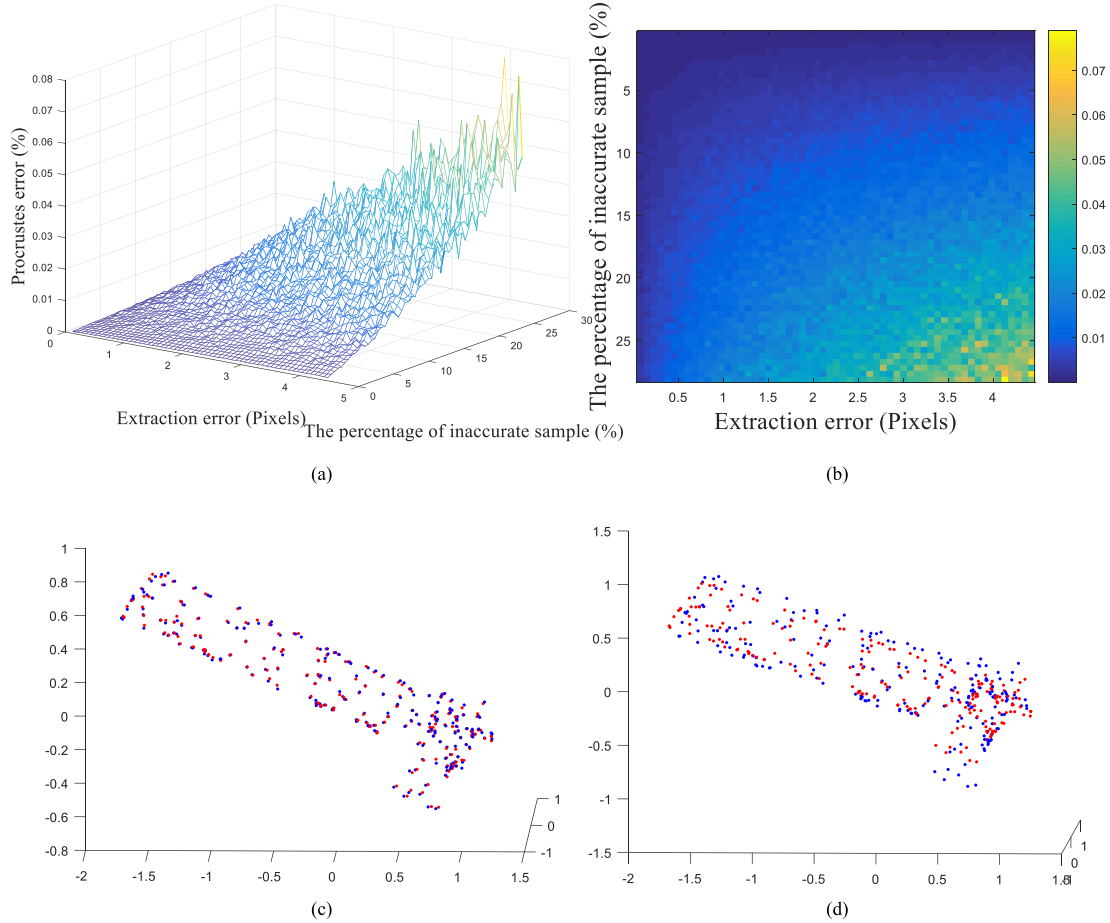


Fig. 8. Target reconstruction results. (a) and (b) Procrustes error of the reconstruction result in different scattering point extraction conditions. (c) Visual reconstruction result when Procrustes error is 0.030. (d) Visual reconstruction result when Procrustes error is 0.045.

the feature association of these scattering points is assumed to be realized, while we use divided facets as surface scatterers to obtain the RD image sequence in Part C.

A. Descriptor Comparison

In this experiment part, we adopt the conventional scattering point feature and the proposed parallelogram feature to describe targets in the same measured ISAR image sequence, respectively. The image sequence is the result of long-time observations of a space shuttle with the TIRA system, which was published by German FGAN Lab in 2012 (@Fraunhofer FHR) [38]. In view of the effectiveness in

TABLE I
Main Parameters of the ISAR System

Size of frames	512×512
Wave length of signal	0.018 m
Bandwidth	1GHz
Center frequency of transmit signal	16.7GHz
Pulse repetition frequency	100Hz

optics image processing, the SIFT algorithm is adopted to extract the scattering point feature in the sequence [39].

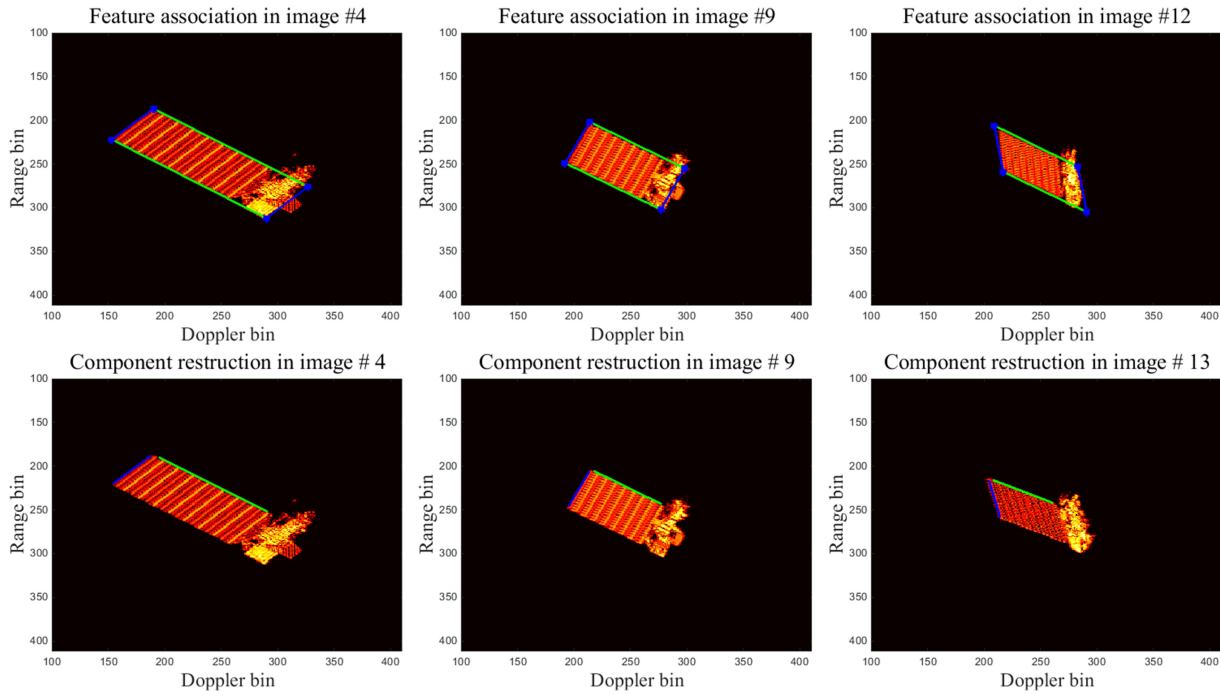


Fig. 9. Experimental results of Pose I. The first row: The extraction and association of the goal component among the ISAR sequence. The second row: The reconstruction images of solar wings (marked green and blue).

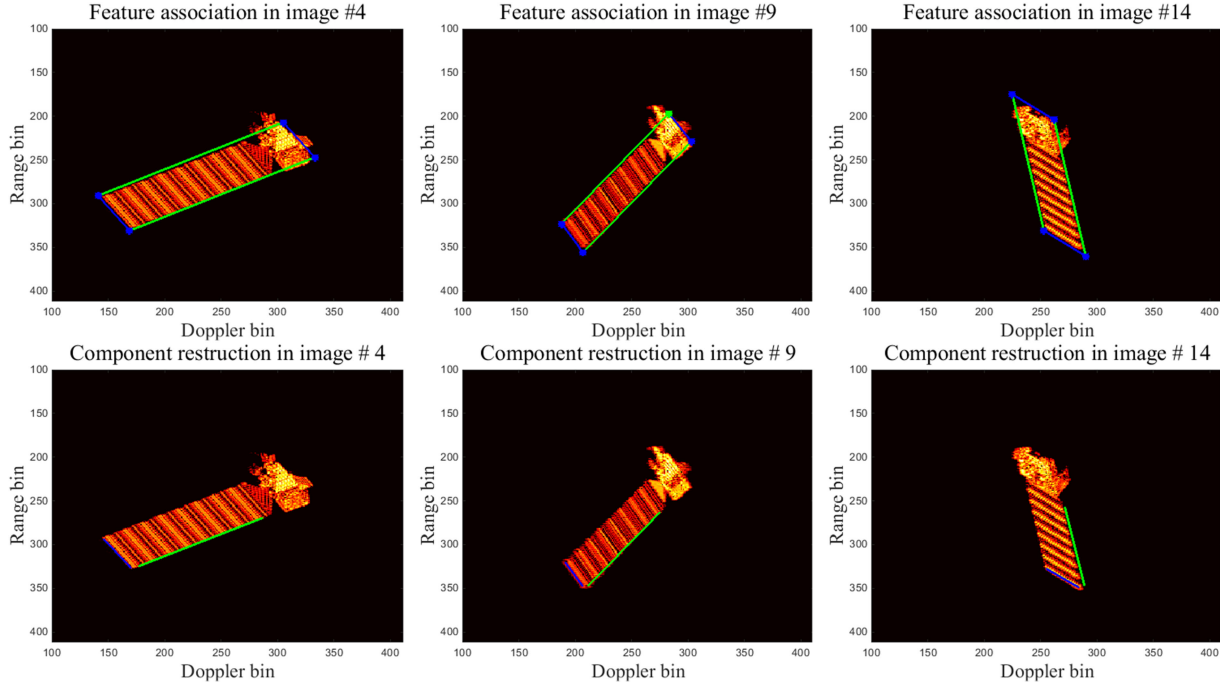


Fig. 10. Experiment results of Pose II. First row: Extraction and association of the goal component among the ISAR sequence. Second row: Reconstruction images of solar wings (marked green and blue).

TABLE II
Estimation Results of the Attitude Parameter

The number of edges	Estimated attitude vector	True attitude vector	Error
The long edge in Pose I	(0.1519,-0.9746,-0.1648)	(0.1526,-0.9744,-0.1650)	0.71 degrees
The short edge in Pose I	(-0.1989,0.1556,-0.9676)	(-0.1986,-0.1413,0.9698)	0.83 degrees
The long edge in Pose II	(0.2480,-0.4504,0.8577)	(-0.2349,0.4663,-0.8529)	1.21 degrees
The short edge in Pose II	(0.0571,-0.8753,-0.4802)	(-0.0649,0.8679,0.4924)	0.93 degrees

TABLE III
Estimation Results of the Component Size Parameter

The number of edges	True size	Estimated size	Error
The long edge in Pose I	15.00 m	14.89m	0.11m
The short edge in Pose I	5.68m	5.70m	0.02m
The long edge in Pose II	15.00 m	14.74m	0.26m
The short edge in Pose II	5.68m	5.71m	0.03m

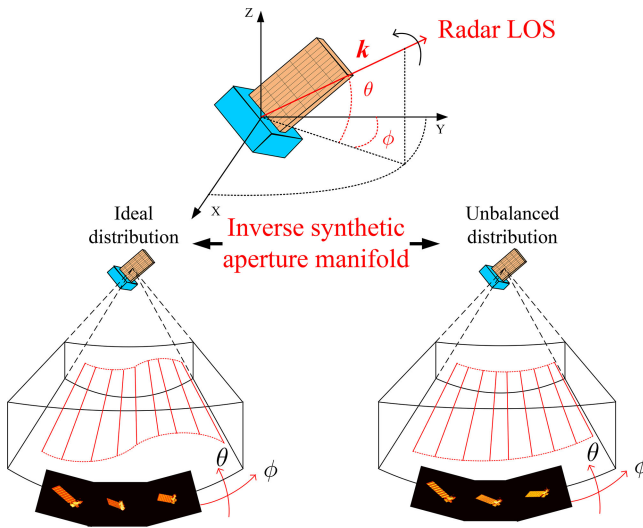


Fig. 11. Inverse synthetic aperture manifold condition analysis of the proposed algorithm.

Fig. 5(a) illustrates the angular glint phenomenon, where scattering points change significantly in adjacent images. As a result, the stability of feature extraction decreases remarkably during the long-time observation. It leads to the missing or association mistakes of key scattering points during the feature association of the image sequence, while the parallelogram descriptor performs well in the same condition, as shown in Fig. 5(b). In practice, the strong consistency of feature extraction usually guarantees the rationality of joint utilizing the sequence information and benefits the deep interpretation of the target state from the image sequence.

B. Target Reconstruction Based on the Factorization Algorithm

We investigated the angular sensitiveness of the scattering point feature in the previous experiment. In this part, the Aura Satellite [40] (see Fig. 6) is adopted as the observed target to analyze the influence of the extraction error of scattering points on the factorization reconstruction algorithm. With a set of low earth orbit (LEO) tracking data, we generate a simulation sequence including 15 point-cloud images, as shown in Fig. 7. After that, 210 facet centers are selected as the feature points and the factorization algorithm in [18] is adopted to rebuild the 3-D distribution of these scattering points. To assess the influence of the feature extraction error, we test the factorization algorithm in different scattering point extraction conditions. The variable

quantities include the extraction error and the percentage of the inaccurate sample, and we quantify the reconstruction performance in terms of the Procrustes error, which is used to account for object scale, rotations, and translations [18].

The experiment of each combination is repeated 30 times to debase the contingency of the reconstruction result. The statistical results are depicted in Fig. 8(a) and (b). We also make a visual comparison between the results of Procrustes error are 0.030 and 0.045, as shown in Fig. 8(c) and (d). It should be emphasized that the lack of axes definition in Fig. 8(c) and (d) reflects the uncertainty of the target attitude and sizes in the target reconstruction result. Thus, Procrustes analysis is used to rotate and change the size of the reconstruction result for matching the original 3-D model, which usually cannot be realized in practical applications.

The visual comparison shows that the insufficient extraction of feature points leads to a serious bias in the 3-D reconstruction by the factorization algorithm. For example, when 15% of the feature points are inaccurate and the extraction bias is less than three pixels, the 3-D target reconstruction fails, as depicted in Fig. 8(d). Moreover, these experiments are all based on the correct association of scattering point features. However, as the previous experiment shows, the association mistake of key scattering points is inevitable in an ISAR image sequence, which adds to the difficulty of the reconstruction based on the factorization approach in practice.

C. Attitude Estimation and 3-D Reconstruction

In this experiment, we utilize the proposed algorithm to estimate the absolute attitude and size parameters of the rectangular component on the target. The simulation adopts a Ku-Band ISAR system and the same LEO tracking data as the former experiment to generate two long-time observation image sequences, where the target attitude is distinctly different. The main parameters of the ISAR system are listed in Table I. Each simulation sequence includes 15 RD images, and the signal-to-noise ratio of each image is 10 dB.

After the image preprocessing, solar wings are extracted as a series of parallelograms and associated among image sequences, as shown in the first rows of Figs. 9 and 10. According to the optimization (16), target attitude parameters are solved by the PSO algorithm. Based on the attitude estimation results given in Table II, the average error of the attitude estimation reaches below 1 degree level, which confirms the accuracy of the proposed algorithm. The angles between the long-edge attitude and the short-edge attitude in the experiments are 91.3° and 90.2° , respectively. It illustrates the effectiveness of the constraint term penalized in the fitness function of (16), which maintains the structural completeness of the target during the attitude estimation. Finally, the attitude estimation result is used for the estimation of size parameters. The results are listed in Table III, and two reconstruction image sequences are generated in the second rows of Figs. 9 and 10. It clearly reveals that the reconstruction of the solar wing is basically consis-

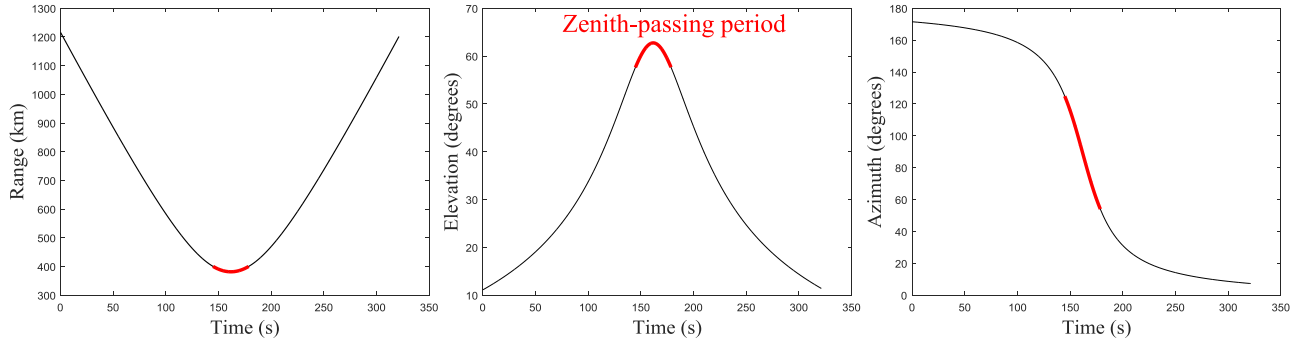


Fig. 12. Orbital condition analysis of the proposed algorithm.

tent with its size in the original image sequence. As shown in Table III, compared with the true sizes in Fig. 6, the estimation result from the proposed method is accurate.

D. Performance Investigation

In all, the attitude estimation results illustrate the effectiveness of the proposed algorithm, and the comparison highlights the advantages of the proposed feature descriptor in the measured data. Besides, although the size estimation relies on the attitude estimation result, the estimation result is fairly close to the true model sizes. The proposed algorithm effectively combines target structural characteristics and the ISAR imaging projection mechanism to interpret target state information, but still has some limitations.

First of all, the solvability of the target attitude depends on the diversity of radar LOS angles. As depicted in Fig. 11, the synthetic aperture geometry manifold expressed by radar imaging projection matrices determines the structure of the optimization function [see (14)]. In the applications, the proposed method generally performs well for the LEO target. Nevertheless, in the case of high earth orbit (HEO) targets, it would fail. The change of the LOS elevation angle θ is inadequate to match up with that of the azimuth angle ϕ for an HEO target, which leads to the unbalanced distribution of attitude parameters in α and β domains. When the observation diversity of LOS angles is significantly insufficient, the optimization function possibly leads to a wrong solution. Meanwhile, in view of ISAR imaging, it would also be difficult to generate a well-focused RD image sequence for HEO targets. Thus, we delimit the application scope of the proposed algorithm for space targets with orbit under 1000 km.

Besides the altitude of the satellite orbit, another external factor is the geometrical relationship of the goal component relative to the inverse synthetic aperture manifold. Normally, a half or third continuous observation astride the zenith-passing period is enough to meet the angular demand of describing the continuous projection change of the rectangular component in different imaging planes. For example, the visible interval of an LEO satellite at an altitude of 400 km might be 10 min for a ground-based radar, as shown in Fig. 12. And a segment of 3–5-min ISAR data is sufficient to meet the angular diversity demand of the

proposed algorithm for the attitude determination. However, we also find some particular combinations of target attitudes, and LOS angles will weaken the parallelogram features in RD images, where the rectangular component is almost projected as a straight line. As a consequence, successful extraction of the component with the parallelogram descriptor would be difficult. The stable association of shape features among the image sequence cannot be ensured, resulting in the failure of the target attitude estimation. Due to the diversity of these combinations, we can hardly find an explicit expression to judge the feasibility of each combination. Nonetheless, an alternative method to handle it is adding other radar stations in practical applications.

On another hand, the performance of image processing also influences the estimation accuracy. In practical applications, the quality of the multisource RD image is various, and the consistency and validity of the observation image sequence are two major principles in image preprocessing. We can draw on the experience of optics image processing and should also take the ISAR image characteristics into consideration, such as the scattering points anisotropy. It is difficult but significant work in radar image interpretation, which we hope will make progress in the future work.

V. CONCLUSION

In this paper, a novel approach was presented to estimate a target's 3-D attitude and rectangular component sizes from an ISAR image sequence. It bridged RD images and the target's motion state, accommodating the ISAR geometric projection model. With the proposed parallelogram feature extracted in the observation image sequence, it recovered the target attitude and rectangular component sizes through a shape priors assistant optimization, which was solved by the PSO algorithm. Comparative experiments illustrated the advantage of the proposed algorithm in feature association, and reconstruction result has confirmed its feasibility. Compared with the existing methods, the proposed approach avoided establishing a simulation database and offered the possibility of attitude estimation for most satellite targets. It should be emphasized that the image processing is usually of difficulties in real ISAR imagery process, which motivates us to seek for a robust image pro-

cessing for precise component extraction. Furthermore, the proposed algorithm is limited to handle the stable satellite. Dynamic estimation of a spinning satellite by exploring its ISAR imagery will be investigated in our further work.

APPENDIX: OPTIMAL OBSERVATION LENGTH SELECTION BASED ON THE LOS PARAMETERS

To ensure the focusing performance of a single ISAR image, LOS angle velocities (θ' and ϕ') within the CPI should be approximate to constants [31], [32]. This requirement can hardly be met in practice, and an acceptable compromise is that the changing rates of θ' and ϕ' should be within definite thresholds during the CPI for each ISAR image frame. Generally, θ and ϕ can be approximated to quadratic curves during a single frame

$$\theta = \theta_0 + \theta' t + \frac{1}{2} \theta'' t^2 = \tilde{\theta} + \Delta\theta(\theta'') \quad (21)$$

$$\phi = \phi_0 + \phi' t + \frac{1}{2} \phi'' t^2 = \tilde{\phi} + \Delta\phi(\phi'') \quad (22)$$

where $\tilde{\theta}$ is the expected value of θ , $\tilde{\phi}$ is the expected value of ϕ , $\Delta\theta(\theta'')$ is the error for θ'' , $\Delta\phi(\phi'')$ is the error for ϕ'' , $t \leq t_{\text{image}}$, and t_{image} is the imaging interval for a single frame.

In the target Cartesian coordinates, the maximum range difference on the target surface can be defined as

$$R(\theta, \phi) = b_x \cos \theta \sin \phi + b_y \cos \theta \cos \phi + b_z \sin \theta \quad (23)$$

where b_x , b_y , and b_z represent coordinates of target size in the target Cartesian coordinate system.

Therefore, the maximum range difference caused by θ'' and ϕ'' can be defined as

$$\begin{aligned} & \Delta R(\theta'', \phi'') \\ &= R(\tilde{\theta} + \Delta\theta(\theta''), \tilde{\phi} + \Delta\phi(\phi'')) - R(\tilde{\theta}, \tilde{\phi}). \end{aligned} \quad (24)$$

Combining (21) and (22), we utilize trigonometric transform and ignore the influence of quadratic term $\Delta\theta(\theta'') \Delta\phi(\phi'')$ to simplify $\Delta R(\theta'', \phi'')$ as (25).

$$\begin{aligned} \Delta R(\theta'', \phi'') &= b_x (\cos \tilde{\theta} \cos \tilde{\phi} \Delta\phi(\phi'') \\ &\quad - \sin \tilde{\theta} \sin \tilde{\phi} \Delta\theta(\theta'')) + b_y (-\sin \tilde{\theta} \cos \tilde{\phi} \Delta\theta(\theta'') \\ &\quad - \cos \tilde{\theta} \sin \tilde{\phi} \Delta\phi(\phi'')) + b_z \cos \tilde{\theta} \Delta\theta(\theta'') \end{aligned} \quad (25)$$

According to the above derivations, it can be noted that in order to achieve an optimal ISAR image of the target, the 2-D rotation angle should be within a small interval. And phase terms $\Delta\varphi(\theta'', \phi'')$ should meet the following condition:

$$\Delta\varphi(\theta'', \phi'') = \left| \frac{4\pi}{\lambda} \Delta R(\theta'', \phi'') \right| \leq \frac{\pi}{4}. \quad (26)$$

ACKNOWLEDGMENT

The authors would like to thank the anonymous reviewers for their valuable comments to improve the paper quality.

REFERENCES

- [1] K. Demars
Nonlinear orbit uncertainty prediction and rectification for space situational awareness
Doctoral dissertation, Dept. Aerosp. Eng. Mech., Univ. Texas Austin, Austin, TX, USA, 2010.
- [2] N. Bobrinsky and L. Monte
The space situational awareness program of the European Space Agency
Cosmic Res., vol. 48, no. 5, pp. 392–398, 2010.
- [3] S. Amico, M. Benn, and J. Jargensen
Pose estimation of an uncooperative spacecraft from actual space imagery
Int. J. Space Sci. Eng. 5, no. 2, pp. 171–189, 2013.
- [4] R. Perrier *et al.*
Satellite image registration for attitude estimation with a constrained polynomial model
In Proc. IEEE Int. Conf. Image Process., 2010, pp. 925–928.
- [5] R. Kanzler *et al.*
Space debris attitude simulation—IOTA (in-orbit tumbling analysis)
In Proc. Adv. Maui Opt. Space Surveillance Technol. Conf., 2015, pp. 1–13.
- [6] J. Silha *et al.*
Apparent rotation properties of space debris extracted from photometric measurements
Adv. Space Res., vol. 61, no. 3, pp. 844–861, 2018.
- [7] F. Santi, D. Pastina, and M. Bucciarelli
Estimation of ship dynamics with a multi-platform radar imaging system
IEEE Trans. Aerosp. Electron. Syst., vol. 53, no. 6, pp. 2769–2788, Dec. 2017.
- [8] L. Yang *et al.*
A 3-D electromagnetic-model-based algorithm for absolute attitude measurement using wideband radar
IEEE Geosci. Remote Sens. Lett., vol. 12, no. 9, pp. 1878–1882, Sep. 2015.
- [9] W. Zhong *et al.*
The attitude estimation of three-axis stabilized satellites using hybrid particle swarm optimization combined with radar cross section precise prediction
Proc. Inst. Mech. Eng. G, J. Aerosp. Eng., vol. 31, no. 2, pp. 222–224, 2015.
- [10] S. Lemmens, H. Krag, and J. Rosebrock
Radar mappings for attitude analysis of objects in orbit
In Proc. 6th Eur. Conf. Space Debris, Darmstadt, Germany, 2013, pp. 20–24.
- [11] G. Li *et al.*
Three-dimensional reconstruction using ISAR sequences
Proc. SPIE, vol. 8919, 2013, Art. no. 891908.
- [12] G. Li *et al.*
A method of 3D reconstruction via ISAR Sequences based on scattering centers association for space rigid object
Proc. SPIE, vol. 9252, 2014, Art. no. 92520N.
- [13] K. Suwa, T. Wakayama, and M. Iwamoto
Three-dimensional target geometry and target motion estimation method using multistatic ISAR movies and its performance
IEEE Trans. Geosci. Remote Sens., vol. 49, no. 6, pp. 2361–2373, Jun. 2011.
- [14] J. Rosebrock
Absolute attitude from monostatic radar measurements of rotating objects
IEEE Trans. Geosci. Remote Sens., vol. 49, no. 10, pp. 3737–3744, Jun. 2011.
- [15] Y. Ma *et al.*
An Invitation to 3-D Vision: From Images to Geometric Models.
Cambridge, MA, USA: Springer, 2012.
- [16] R. Hartley, A. Zisserman, and T. Jin

- Multiple View Geometry in Computer Vision*. Cambridge, MA, USA: Cambridge, 2003.
- [17] E. Mcfadden *et al.* Three-dimensional reconstruction from ISAR sequences In *Proc. AeroSense Int Soc. Opt. Photon.*, 2002, pp. 58–67.
- [18] M. Ferrara, G. Arnold, and M. Stuf Shape and motion reconstruction from 3D-to-1D orthographically projected data via object image relations *IEEE Trans. Pattern Anal. Mach. Intell.*, vol. 31, no. 10, pp. 1906–1912, Oct. 2009.
- [19] M. Ferrara *et al.* Robust estimation of shape invariants In *Proc. Radar Conf.*, 2012, pp. 0167–0172.
- [20] C. Tomasi and T. Kanade Shape and motion from image streams under orthography: A factorization method *Int. J. Comput. Vis.*, vol. 9, no. 2, pp. 137–154, 1992.
- [21] F. Wang, F. Xu, and Y. Jin 3-D information of a space target retrieved from a sequence of high-resolution 2-D ISAR images In *Proc. IEEE Int. Geosci. Remote Sens. Symp.*, 2016, pp. 5000–5002.
- [22] J. Lindsay Angular glint and the moving, rotating, complex radar target *IEEE Trans. Aerosp. Electron. Syst.*, vol. AES-4, no. 2, pp. 164–173, Mar. 1968.
- [23] H. Yin and P. Huang Further comparison between two concepts of radar target angular glint *IEEE Trans. Aerosp. Electron. Syst.*, vol. 44, no. 1, pp. 372–380, Jan. 2008.
- [24] J. Mayhan *et al.* High resolution 3D ‘snapshot’ ISAR imaging and feature extraction *IEEE Trans. Aerosp. Electron. Syst.*, vol. 37, no. 2, pp. 630–642, Apr. 2001.
- [25] J. Kennedy and R. Eberhart Particle swarm optimization In *Proc. IEEE Int. Conf. Neural Netw.*, 2002, vol. 4, pp. 1942–1948.
- [26] B. Riwanto *et al.* Particle swarm optimization with rotation axis fitting for magnetometer calibration *IEEE Trans. Aerosp. Electron. Syst.*, vol. 53, no. 2, pp. 1009–1022, Apr. 2017.
- [27] O. Montenbruck, E. Gill *Satellite Orbits: Models, Methods and Applications*. Cambridge, MA, USA: Springer, 2012.
- [28] Y. Zhang and Y. Zhong Calculation of subsatellite track of remote sensing satellite in nearly round orbit *J. Inst. Surveying Mapping*, vol. 18, no. 4, pp. 257–269, 2001.
- [29] X. Ning, C. Ye, and J. Yang Radar aspect angle rate-of-change with respect to space target and its application *J. Tsinghua Univ. (Sci. Technol.)*, vol. 53, no. 11, pp. 1029–1040, 2013.
- [30] J. Walker Range-Doppler imaging of rotating objects *IEEE Trans. Aerosp. Electron. Syst.*, vol. AES-16, no. 1, pp. 23–52, Jan. 1980.
- [31] Z. Bao, M. Xing, and T. Wang *Radar Imaging Technology*. Beijing, China: Publishing House of Electronics Industry, pp. 24–40, 2005.
- [32] G. Ettinger and W. Snyder Model-based fusion of multi-look SAR for ATR *Proc. SPIE*, vol. 4727, pp. 277–289, 2002.
- [33] P. Svigny and D. Difilippo A multi-look fusion approach to through-wall radar imaging In *Proc. Radar Conf.*, 2013, pp. 1–6.
- [34] C. Rafael, Gonzalesz, and E. Richard *Digital Image Processing*. Beijing, China: Publishing House of Electronics Industry, 2007, pp. 432–435.
- [35] S. Deans *The Radon Transform and Some of Its Applications*. North Chelmsford, MA, USA: Courier Corporation, 2007.
- [36] F. Angel, A. Omar, and G. Jesus Facet model of moving targets for ISAR imaging and radar back-scattering simulation *IEEE Trans. Aerosp. Electron. Syst.*, vol. 46, no. 3, pp. 1455–1467, Jul. 2010.
- [37] F. Wang, F. Thomas, and Y. Jin Simulation of ISAR imaging for a space target and reconstruction under sparse sampling via compressed sensing *IEEE Trans. Geosci. Remote Sens.*, vol. 53, no. 6, pp. 3432–3441, Jun. 2015.
- [38] 2010. [Online]. Available: <https://www.fhr.fraunhofer.de/de/das-institut/technische-ausstattung/weltraumbeobachtungsradartira>
- [39] D. Lowe Distinctive image features from scale-invariant keypoints *Int. J. Comput. Vis.*, vol. 60, no. 2, pp. 91–110, 2004.
- [40] 2016. [Online]. Available: <https://avdc.gsfc.nasa.gov>
- [41] D. Kucharski *et al.* Attitude and spin period of space debris Envisat measured by satellite laser ranging *IEEE Trans. Geosci. Remote Sens.*, vol. 52, no. 12, pp. 7651–7657, Dec. 2014.
- [42] S. Sommer *et al.* Temporal analysis of Envisats rotational motion *J. Brit. Interplanet.*, vol. 70, pp. 45–51, 2017.



Yejian Zhou was born in Zhejiang Province, China, in 1993. He received the B.S. degree in electronic engineering in 2015 from Xidian University, Xi'an, China, where he is currently working toward the Ph.D. degree in signal processing with the National Laboratory of Radar Signal Processing.

His research interests include inverse synthetic aperture radar imaging and image interpretation.



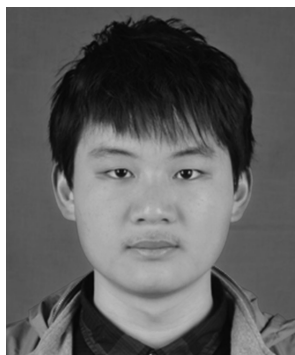
Lei Zhang was born in Zhejiang Province, China, in 1984. He received the Ph.D. degree in electronic engineering from Xidian University, Xi'an, China, in 2012.

He is currently an Associate Professor with the National Laboratory of Radar Signal Processing, Xidian University. He is also with the School of Electronics and Communication Engineering, Sun Yat-Sen University, Guangzhou, China. His research interests include radar imaging (synthetic aperture radar/inverse synthetic aperture radar) and motion compensation.



Yunhe Cao was born in Anhui Province, China. He received the B.S., M.S., and Ph.D. degrees in electronic engineering from Xidian University, Xi'an, China, in 2001, 2004, and 2006, respectively.

He is currently a Professor with the National Laboratory of Radar Signal Processing, Xidian University. His research interests include multiple-input multiple-output radar, digital array radar, adaptive signal processing, and target detection.



Zhenhua Wu was born in Anhui Province, China, in 1993. He received the B.S. degree in electronic engineering in 2014 from Xidian University, Xi'an, China, where he is currently working toward the Ph.D. degree in signal processing with the National Laboratory of Radar Signal Processing.

His research interests include radar imaging and sparse signal processing.